ARTICLE

Check for updates

# Fish-inspired flexible protective material systems with anisotropic bending stiffness

Katia Zolotovsky[1,4,7], Swati Varshney [2,7], Steffen Reichert[1,2,5], Eric M. Arndt [2], Ming Dao[2], Mary C. Boyce[3,6] & Christine Ortiz[2 ✉]

Biological structures integrate morphometry (shape-based rules) with materials design to maximize organism survival. The exoskeleton of the armored fish, *Polypterus senegalus*, balances flexibility with protection from predatory and territorial threats. Material properties of the exoskeleton are known; however, the geometric design rules underlying its anisotropic flexibility are uncharacterized. Here, we show how scale shape, articulation, and composite architecture produce anisotropic mechanics using bio-inspired, multi-material 3D-printed prototypes. Passive loading (draping) shows that compliant connections between the scales contribute to mechanical anisotropy. Simulated and experimental active loading (bending) show orientation-dependent stiffness ranging over orders of magnitude, including 'mechanical invisibility' of the scales where they do not add stiffness to the exoskeleton. The results illustrate how morphometry provides a powerful tool to tune flexibility in composite architectures independent of varying constituent materials composition. We anticipate that introducing morphometric design strategies will enable flexible, protective systems tuned to complex shapes and functions.

[1]Department of Architecture and Planning, Massachusetts Institute of Technology, Cambridge, MA, USA. [2]Department of Materials Science and Engineering, Massachusetts Institute of Technology, Cambridge, MA, USA. [3]Department of Mechanical Engineering, Massachusetts Institute of Technology, Cambridge, MA, USA. [4]Present address: Division of Experimental and Foundational Studies, Rhode Island School of Design, Providence, RI, USA. [5]Present address: Institute for Computational Design, Faculty of Architecture and Urban Planning, University of Stuttgart, Stuttgart, Germany. [6]Present address: School of Engineering and Applied Sciences, Columbia University, New York, NY, USA. [7]These authors contributed equally: Katia Zolotovsky, Swati Varshney. ✉email: cortiz@mit.edu

Many animals have evolved hard exoskeletons to resist predation or competitive attacks (e.g., crustaceans[1], insects[2], mollusks[3], turtles[4,5], seahorses[6,7], and bony fish[8–10]). These 'natural armors' combine micro- and nano-scale materials design (e.g., materials selection, crystallography, composite architecture, porosity, surface chemistry) with macroscale geometrical design rules[11–15] to provide additional functionalities[16] such as enhanced mechanical properties[17,18], transparency[19], or flexibility[20,21]. Fish possess highly flexible armored exoskeletons which have attracted particular interest in the field of bio-inspired design[22–24]. The armored fish *Polypterus senegalus* (bichir) possesses an exoskeleton of imbricated, articulating, mineralized scales that provides penetration resistance from predatory and territorial attacks while granting the fish serpentine mobility[25–28]. While the complex geometry of the scales, their shape variation along the body length, and their protective capabilities have been studied[20,27,29–32], there has yet been no comprehensive analysis of the geometric design rules, such as scale geometry, local articulation, and global assembly.

Here, we integrate advances in microtomographic imaging, parametric modeling, and multi-material 3D printing to achieve three goals: (1) translate the hierarchical geometric rules of assembly in the *P. senegalus* exoskeleton to a synthetic, flexible composite prototype, (2) experimentally and computationally assess the prototype's mechanical behavior, and (3) elucidate the structure–function relationships that determine how shape of individual components can be used as a materials design parameter to tune the anisotropic behavior of composite materials. Parametric 3D modeling was used to design bio-inspired prototypes by generating abstracted models of scales from x-ray microtomography data and integrating the multi-material components into the flexible composite assembly. Multi-material 3D printing was used to fabricate the bio-inspired flexible armor prototypes. Anisotropic flexibility of the prototypes was examined under passive loading (self-weight). A mechanical tester was used to quantify the bending stiffness of the prototypes in active loading (bending), and finite element simulations were developed to correlate internal stress concentrations with mechanical response.

The results show how the complex scale shape contributes to local interscale mobility mechanisms that determine the bending response of the global prototype and generate anisotropic mechanical behavior. The most flexible orientations, including one in which the scales are 'mechanically invisible' without adding stiffness to the armor assembly, correspond to physiologically relevant bending modes in the fish. With one prototype design scheme, a wide array of mechanical behavior was generated with stiffness ranging over several orders of magnitude, thus showing how morphometry can tune the flexibility of protective, composite architectures without varying the constituent materials or their volume fractions. We anticipate that the introduction of geometric variation into synthetic prototypes will generate flexible, protective systems that are well adjusted to complex shapes, kinematics, and functional differentiations[33].

Results

Translation of the geometric rules of assembly to a bio-inspired prototype.
The *P. senegalus* exoskeleton covers the entire surface of the fish from head to tail. The scales are arranged in helical columns that wind around the body, with an angle (β) of 60° between the helical, paraserial axis and the horizontal plane in a straight body posture, shown in the schematic in Fig. 1a. Segmentation of the scales, their complex geometry, and their joint articulation mechanisms allow the fish to achieve large, bi-directional body curvatures in axial bending (Fig. 1b).

P. senegalus scales were scanned using x-ray microtomography (μCT) to generate reconstructed, digital 3D models. The shape and size of scales vary gradually across the fish exoskeleton, so in order to produce a tileable scale geometry, μCT data from an adjacent pair of scales were combined into a unitized scale shown in Fig. 2a. The individual scale geometry is complex with distinct features including the peg (P), socket (S), anterior process (AP), anterior shelf (AS), concave anterior margin (AM), and a thickened axial ridge (AR). Scales use two primary joints to interact with their neighbors and form an assembly in the exoskeleton (Fig. 2b–c): the articulated peg-and-socket joint in the paraserial direction within a column of scales, and the sliding overlap joint in the interserial direction between columns of scales situated at the angle β away from the paraserial axis.

Collagenous Sharpey's fibers run between the peg and socket of adjacent scales to reinforce the joint, and a collagenous, multi-layered fibrous *stratum compactum* attaches the scales to the underlying soft tissue dermis at the axial ridge[27]. A portion of the protective exoskeleton shown is in Fig. 2d.

Prototypes were designed using computer-aided design (CAD) software to render the individual scale geometry into an abstracted 3D model (Fig. 2e) of 20 mm length with an overall rhomboid shape allowing for a tapered overlap area between scales, a tetrahedral peg, and a corresponding inverted concave socket. Parametric modeling was used to replicate the abstracted scale into a 2D array which preserved the joint articulation mechanisms with $\beta = 60°$ between the paraserial and interserial axes (Fig. 2f–h). An underlying substrate was added, and the two compliant connective tissue elements were then integrated into the model as paraserial scale connections and attachments between the scale and the substrate (Fig. 2f).

The translated 3D designs were fabricated by multi-material inkjet 3D printing, using VeroWhite photopolymer (hard plastic with elastic modulus (E) = 2.0 GPa[34,35]) for the scales and TangoPlus photopolymer (rubber-like elastomer with E = 0.63 MPa[34,35]) for the soft components (Sharpey's fibers, stratum compactum, and underlying tissue) to yield synthetic, flexible composite prototypes (Fig. 2i). We choose this 3D printing technique due to its significant advantages over other fabrication techniques[21,22], including high resolution and dimensional accuracy, ease of producing arbitrary multi-material 3D structures, and the large stiffness ratio between different photopolymers (order of ~10^4). This stiffness ratio reasonably agrees with the expected physiological value (order of ~10^3) based on representative stiffnesses of mineralized (bone, ~10 GPa) and soft (collagen, ~10 MPa) biological tissues. The distance between the scales in the 3D printed prototypes is 1 mm, approximately thirty times larger compared to the resolution of the printer (30 microns), which ensures the soft connections between the scales are resolved.

Anisotropic flexibility is governed by paraserial connectivity.
The innate flexibility of the prototype under passive loading (self-weight) was examined by draping a prototype comprising a square array of seventy two 20 mm scales over a half-cylinder mold with radius of curvature (R_m) without the application of an external load (Fig. 3). To ensure that our biomimetic model can address the full range of flexibility of the fish, we chose the ratio of scale size to the mold radius of curvature to equal the ratio of physiological scale size to the maximum physiological radius of curvature calculated from the reported curvature value[27].

The flexibility of the prototype, as shown by the calculated radius of curvature (R_p), varied with the orientation of the scales over the mold (Fig. 3a–d). The radius of curvature of the prototype relative to the radius of curvature of the mold (R_p/R_m)
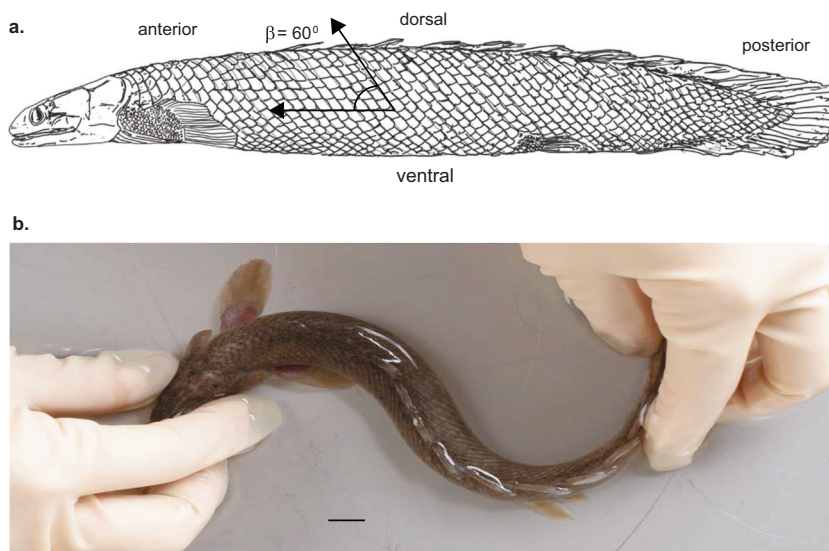
Fig. 1 The *P. senegalus* exoskeleton. a Schematic of the left side of a fish showing the helical arrangement of scales with angle $\beta = 60°$ between the helical (paraserial) axis and the horizontal plane (sketch by the authors). **b** Anesthetized *P. senegalus* specimen (body length = 219 mm) exhibiting bi-directional body curvature in axial bending. Scale bar = 10 mm.

is plotted against orientation angle (α) in Fig. 3e ($N = 3$ per sample). The prototype attains maximum flexibility at $\alpha = 0°$ where the paraserial peg-and-socket axis is aligned with the mold's axis of zero curvature (Fig. 3f); the overlap joint allows the columns of scales to slide away from each other without resistance, and the prototype completely conforms to the mold with $R_p = R_m$. The radius of curvature of the prototype increased with α until reaching a maximum rigidity at $\alpha = 90°$, where the peg-and-socket joint was aligned along the axis of mold curvature (Fig. 3d, g); the articulated peg-and-socket joint restricts the motion of scales within the column of scales, and thus resists flexure of the prototype so that it lies almost flat above the mold with $R_p = 4.2R_m$. As the prototype was rotated past $\alpha = 90°$, the peg-and-socket joint returns to alignment with the mold's line of zero curvature, and the global flexibility returns. A second prototype was designed without the paraserial connective elements between the peg and socket of neighboring scales. This prototype assembly exhibited uniformly maximal flexibility in all orientations, mechanically equivalent to the flexible substrate without scales (Fig. 3e). The results suggest that collagenous Sharpey's fibers are a critical structural component in restricting the ranges of motion between scales at the peg-and-socket joint, thereby increasing the resistance to flexure along the paraserial axis and introducing mechanical anisotropy to the system.

Interscale mobility mechanisms and the bending stiffness. We tested bioinspired flexible composite prototypes in active loading (bending) to examine how scale shape contributes to local interscale mobility mechanisms and generates anisotropic mechanical behavior (Fig. 4a–c).

Reaction force (F) vs. vertical displacement (d) for the prototypes ($N = 3$ per orientation) is plotted in Fig. 4d. Each orientation (φ) has a characteristic loading response which can be divided into phases. Stiffness ($\underline{K}$) for each phase, plotted in Fig. 4e, is calculated as the slope of the loading curve and normalized by the stiffness of a control sample with no scales, comprising TangoPlus elastomer only. The scale-less prototype was chosen as the control as it represents an integument without protective scales, which would be expected to have maximum flexibility (lowest stiffness). Stiffness and interscale mechanisms observed in each loading phase of each orientation are tabulated

Table 1 Displacement range, stiffness ($\underline{K}$), and interscale mobility mechanisms for each loading phase of each prototype orientation (φ).

φ	Phase	Displacement (mm)	$\underline{K}$	Mechanism(s)
$0°$	I	0–5	47.8	paraserial bending
	II	5–85	15.8	paraserial + interserial rotation
$30°$	I	0–5	126	paraserial bending
	II	5–15	21.7	paraserial rotation
	III	15–85	<0	paraserial failure
$60°$	I	0–5	31.3	interserial sliding
	II	5–85	10.5	paraserial + interserial rotation
$90°$	I	0–5	0.99	interserial sliding
	II	5–85	4.23	interserial sliding
$120°$	I	0–5	124	interserial sliding
	II	5–15	46.8	paraserial + interserial rotation
	III	15–85	24.1	interserial splay
$150°$	I	0–5	452	paraserial rotation
	II	5–35	80.9	paraserial + interserial rotation, interserial splay
	III	35–85	21.4	paraserial bending

in Table 1. Finite element (FE) models of the prototypes were also created to computationally simulate bending (Fig. 5). The interscale mobility mechanisms that contribute to the mechanical response of the global assembly are depicted in Fig. 6.

In the $\varphi = 0°$ orientation, the paraserial axis of the scales is aligned with the loading direction. In the first phase, the scales undergo paraserial bending as the compliant TangoPlus connection within the peg-and-socket joint resists deformation ($\underline{K} = 47.8$, Table 1). In the second phase, the scales interlock paraserially (Fig. 5a.i), generating stress concentrations around the peg and socket (Fig. 5a.ii). The paraserial interlock causes paraserial rotation as the anterior margin rotates toward the substrate, coupled with interserial rotation when the anterior process pushes into the substrate (into plane) and the back of the anterior margin and socket lifts up (out of plane) (6a, 6b.i–ii). At
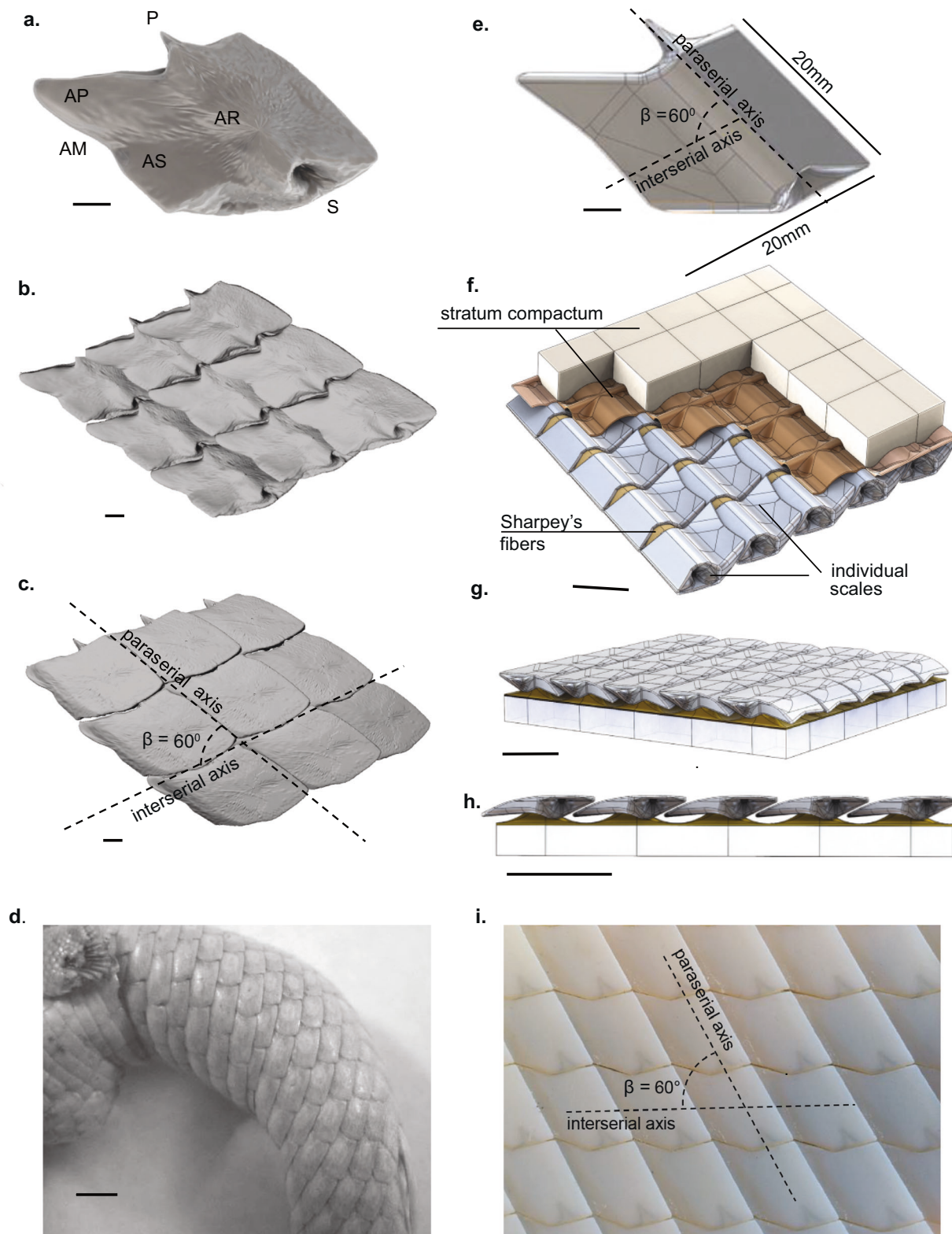
Fig. 2 Translation of the biological design rules to a synthetic flexible composite material. a 3D μCT reconstruction of an averaged scale highlighting geometrical features: peg (P), socket (S), anterior process (AP), anterior shelf (AS), concave anterior margin (AM), and axial ridge (AR). Scale bar = 1 mm. **b** Homogeneous assembly of the biological scale geometry, interior view (scale bar = 1 mm), and **c** exterior view, showing the paraserial and interserial axes oriented at angle β = 60° from each other. Scale bar = 1 mm. **d** A photograph of the biological exoskeleton in a deceased *P. senegalus* specimen. Scale bar = 5 mm. **e** Abstracted geometry (3D model) of a single scale unit magnified to 20 mm length. Scale bar = 1 mm. **f** Associative 3D model of the scale assembly that incorporates the essential parts of the exoskeletal assembly, including the scales, substrate, paraserial connections, and scale–substrate attachment, interior view (scale bar = 20 mm), **g** exterior view (scale bar = 20 mm), and **h** cross-sectional view. Scale bar = 20 mm. **i** A photograph of a multi-material 3D-printed prototype of the scale assembly.
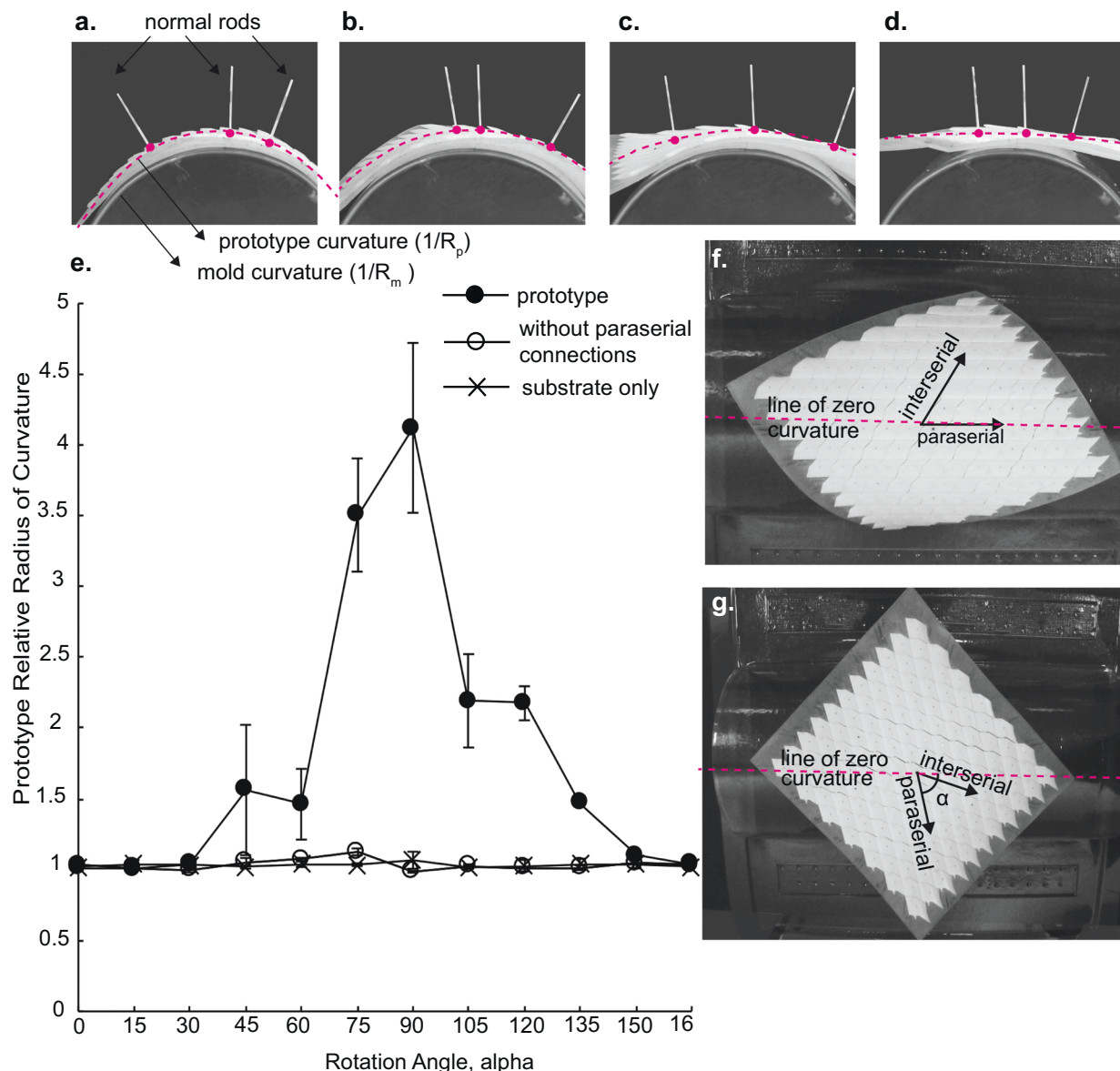
Fig. 3 Anisotropy of prototype flexibility measured by radius of curvature. a Prototype with an array of 72 scales is draped over a half-cylinder mold at angle (α) = 0° between the prototype's paraserial axis and the mold's line of zero curvature. Lines show the curvature of the mold (white) and prototype (red). Inverse of curvature represents the radius of curvature of the prototype (R_p) and the radius of curvature of the mold (R_m). The prototype exhibits different curvatures when rotated to **b** α = 30°, **c** α = 60°, **d** α = 90°. **e** Relative radius of curvature (R_p/R_m) vs. α for the prototype, a variation without the paraserial connections, and the substrate only. Error bars represent standard deviation with N = 3 samples per prototype design. **f** Top view of the prototype in the α = 0° orientation. **g** Top view of the prototype in the α = 90° orientation.

large deformations, the high internal stresses are distributed throughout the body of the scales (Fig. 5a.iii).

In the φ = 30° orientation, the scales initially undergo paraserial bending ($\underline{K}$ = 126) until paraserial interlock (Fig. 6b.iii). The interlock causes small paraserial rotation alongside paraserial bending as the anterior margin rotates into plane (Fig. 6b.iii). The orientation of the scales gives tolerance to the anterior process so that it is not pushed into substrate; there is no coupling with interserial rotation, and the stiffness drops ($\underline{K}$ = 21.7). As the model bends, stresses form at the sites of paraserial, interscale contact around the peg and socket of adjacent scales; the stresses grow and become distributed over the scale surface with higher degrees of bending (Fig. 5b.i–iii). At large deformations, paraserial failures occur in parallel throughout the sample (Fig. 5b.iii), after which the prototype offers no resistance to global bending ($\underline{K}$ < 0).

In the φ = 60° orientation, the scales first undergo interserial sliding as the anterior shelf slides under the scale in the adjacent column without generating any stresses on the scales (Fig. 5c.i). The oblique angle of orientation then causes the scales to touch interserially and resist deformation ($\underline{K}$ = 31.3) while generating stresses at the site of contact (Fig. 5c.ii). As the sample continues to bend, the interserial interlock causes small paraserial rotation (anterior margin moves out of plane) coupled with large interserial rotation (anterior process moves out of plane; back of anterior margin and socket move into plane) to accommodate interserial sliding (Fig. 6b.iv). Stresses grow at the sites of interscale contact and spread throughout the body of the scales (Fig. 5c.iii). The compliant paraserial connections resist the rotations but do not break, so the prototype is able to bear load as it bends ($\underline{K}$ = 10.5).

In the φ = 90° orientation, the paraserial axis is perpendicular to the loading direction. In bending, the columns of scales move
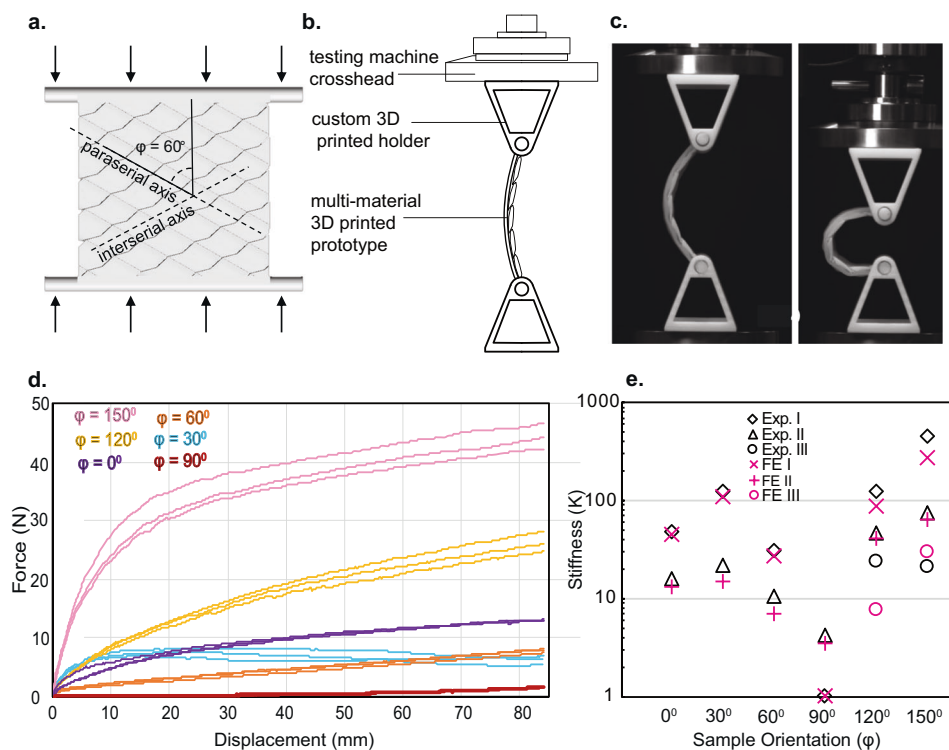
Fig. 4 Anisotropic bending stiffness of the flexible composite prototypes. a Rendered front view of the prototype designed for bending with rigid rods at the top and bottom and with the paraserial axis oriented at an angle (φ) = 60° away from the loading direction. **b** Schematic drawing of the sample holder. **c** Side view of the φ = 60° sample loaded in bending at various vertical displacements (*d*): *d* = 20 mm (left) and *d* = 80 mm (right). **d** Force–displacement curves for prototypes with φ = 0°, 30°, 60°, 90°, 120°, and 150°. **e** Normalized stiffness (*K*) of each phase of each prototype's loading curve (experiments and finite element simulations). Error bars represent standard deviation with *N* = 3 samples per prototype orientation.

relative to each other via interserial sliding (Fig. 5d.i, 6b.v), and the only resistance to bending comes from the tensile stresses in the substrate beneath the scales. Here, the rigid scales are 'mechanically invisible' as they do not contribute any resistance to bending, and the sample's stiffness matches that of the substrate (*K* = 0.99). At large degrees of deformation, the scales begin to touch interserially (Fig. 6b.v, vi). The scale contacts cause the columns of scales to rotate about the axial ridge, further straining the compliant material at the site of attachment to the substrate and introducing stresses into the center of the scales (Fig. 5d.ii–iii). As a result, the stiffness of the sample increases (*K* = 4.23).

When the φ = 120° prototype bends, the scales first move via interserial sliding. However, the anterior process is pushed into the substrate immediately, and these contacts induce paraserial rotation (anterior margin moves into plane) coupled with interserial rotation (anterior process and peg move into plane; back of anterior margin and socket move out of plane) to generate additional paraserial and interserial scale contacts (Fig. 6b.vii–viii) that in turn generate high stiffness (*K* = 124). Stress concentrations form on the scales in regions surrounding the peg and socket where paraserial contacts occur (Fig. 5e.i), at the sites of interserial contact between the columns of scales (Fig. 5e.ii), and throughout the substrate where the anterior process pushes in. These scale interlocks contribute to the high stiffness with further bending (*K* = 46.8). At very large deformations, the scales splay interserially (Fig. 5e.iii) to further accommodate sliding with reduced stiffness (*K* = 24.1).

The φ = 150° prototype is the stiffest of all orientations. At the onset of bending, small degrees of paraserial bending causes the anterior process to push into the substrate immediately

while the back end of the anterior margin impinges on the scale in the adjacent column. These scale contacts do not allow for further paraserial bending, provide no tolerance for interserial sliding, and cause high stiffness (*K* = 450). With further bending, the scale contacts cause paraserial rotation (anterior margin moves into plane) coupled with interserial rotation (Fig. 6b.ix); however, the interlocked scales continue to resist bending with high stiffness (*K* = 80.9) and high stresses are sustained at the sites of contact between scales and spread throughout selective columns of scales (Fig. 5f.i–ii). At very large deformations, the scale interlocks resist bending such that the rods which are inserted into the sample holders bow out to accommodate the deformation with high stresses throughout the model (Fig. 5f.iii). Eventually, the compliant paraserial interconnections start to tear, and small degrees of paraserial bending are observed, while the scale interlocks allow the prototype to sustain high loads (*K* = 21.4).

For all orientations, the measured stiffnesses *K* are less than what would be expected from a rule-of-mixtures combination (i.e., homogeneous blend) of the rigid and soft photopolymers. The volume percent of stiff (VeroWhite, 2.0 GPa) and compliant (TangoPlus, 0.63 MPa) materials in the printed prototypes were 46% and 54%, respectively, after removal of support material, so the rule-of-mixtures expected stiffness of a homogenous blend is 0.92 GPa (predicted *K* = 1460), similar to a semirigid plastic such as high density polyethylene, which would not be expected to provide measurable drapability in the passive loading test. This demonstrates the importance of the segmentation of the integument into discrete, morphometrically complex scales in order to achieve anisotropic flexibility while providing protection.
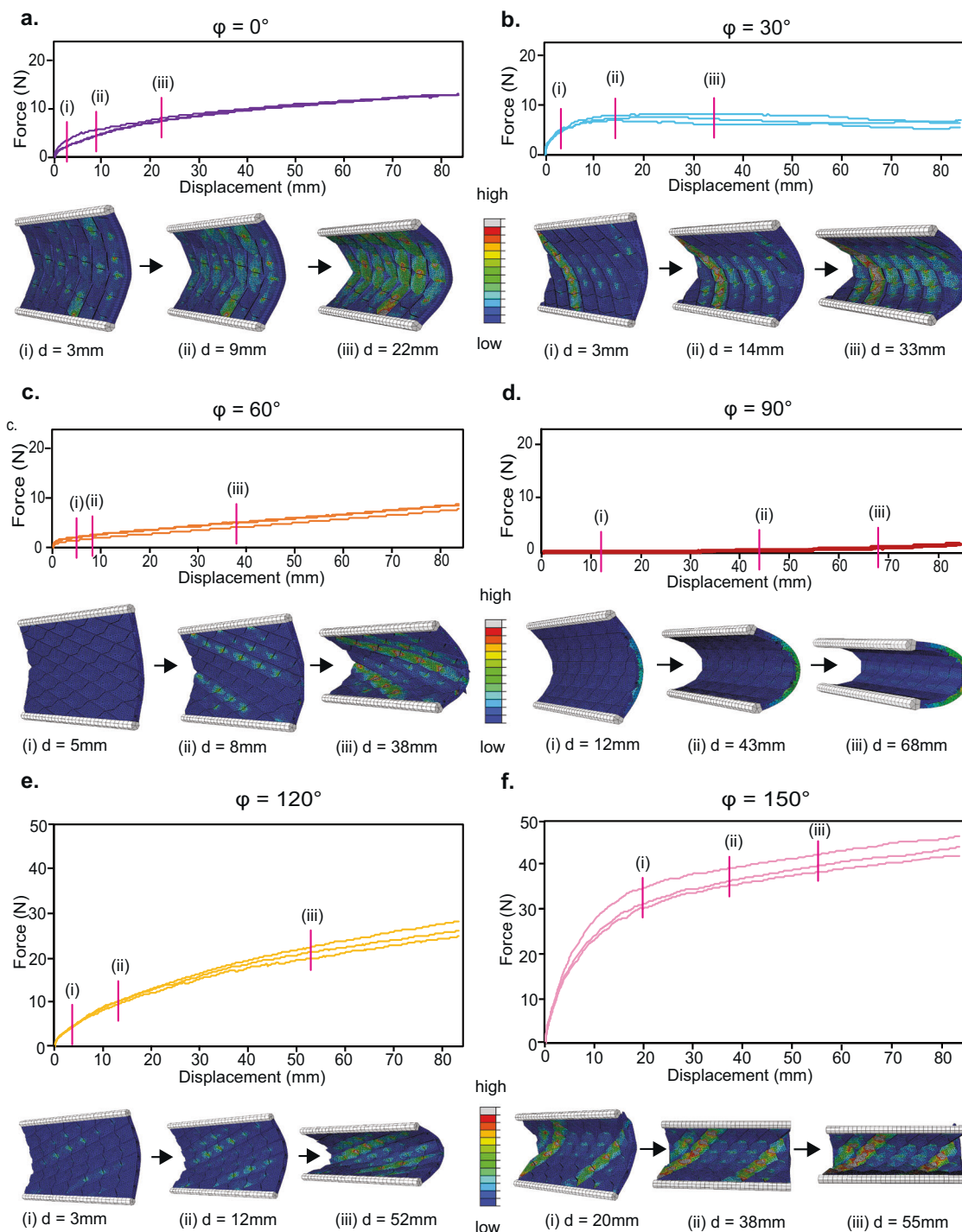
Fig. 5 Orientation-dependent bending behavior of the scaled prototypes. a Experimental bending of the prototype with $\varphi = 0°$. Stress plots (Mises, linear elastic) from the FE simulation of the $\varphi = 0°$ model. (i) Front view at $d = 3$ mm, (ii) $d = 9$ mm, and (iii) $d = 22$ mm. **b** Experimental bending of the prototype with $\varphi = 30°$. Stress plots, front view at (i) $d = 3$ mm, (ii) $d = 14$ mm, and (iii) $d = 33$ mm. **c** Experimental bending of the prototype with $\varphi = 60°$. Stress plots, front view at (i) $d = 5$ mm, (ii) $d = 8$ mm, and (iii) $d = 38$ mm. **d** Experimental bending of the prototype with $\varphi = 90°$. Stress plots, front view at (i) $d = 12$ mm, (ii) $d = 43$ mm, and (iii) $d = 68$ mm. **e** Experimental bending of the prototype with $\varphi = 120°$. Stress plots, front view at (i) $d = 3$ mm, (ii) $d = 12$ mm, and (iii) $d = 52$ mm. **f** Experimental bending of the prototype with $\varphi = 150°$. Stress plots, front view at (i) $d = 20$ mm, (ii) $d = 38$ mm, and (iii) $d = 55$ mm.

Discussion

A hierarchy of shape- and materials-based design principles were translated from the biological exoskeleton of *P. senegalus* and integrated into the bioinspired flexible composite prototypes, including the complex shape of rigid scales, interscale joint articulation structure, assembly of scales into an armored surface, and soft connective components (substrate, scale-to-substrate attachment, and paraserial connections). The prototypes were able to replicate the biomechanical behavior of the biological exoskeleton, where the complex scale shape and joint articulations contribute to local, interscale mobility mechanisms that in turn determine the bending response of the global sample,
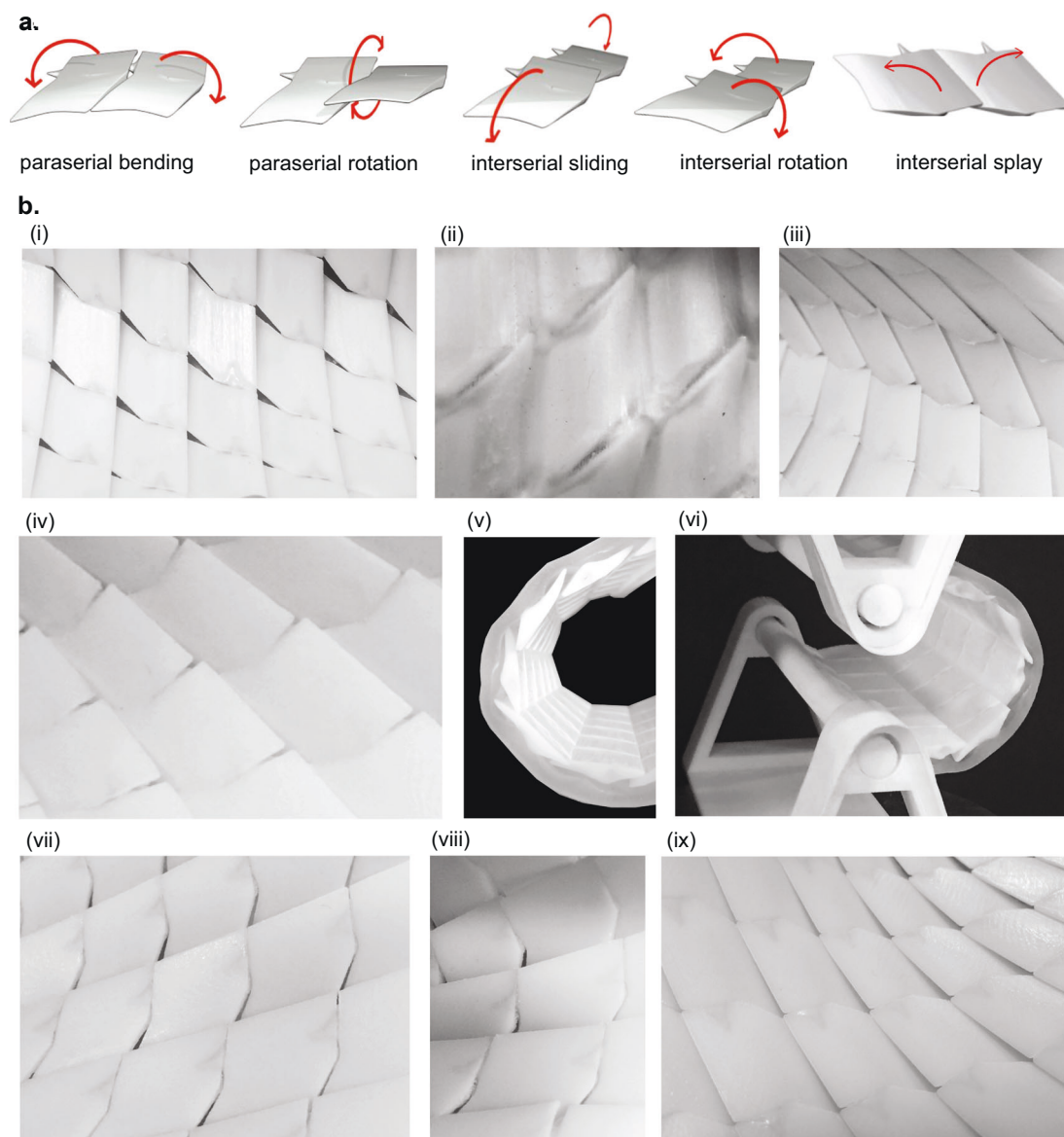
Fig. 6 Orientation-dependent bending behavior of the scaled prototypes. a Schematics of the six interscale mobility mechanisms observed during bending. **b** Experimental bending of the prototype with (i) $\varphi = 0°$. Paraserial bending at vertical displacement (d) = 3 mm and (ii) back view of sample showing anterior process pushing into the substrate at $d = 15$ mm. (iii) $\varphi = 30°$. Paraserial rotation at $d = 15$ mm. (iv) $\varphi = 60°$. Paraserial and interserial rotation at $d = 50$ mm. (v) $\varphi = 90°$. Interserial sliding at $d = 15$ mm, side view and (vi) further interserial sliding after interserial contacts at $d = 60$ mm (side view). (vii) $\varphi = 120°$. Paraserial and interserial rotations and (viii) interscale contacts at $d = 20$ mm. (ix) $\varphi = 150$. Paraserial and interserial rotations plus interserial splay at $d = 14$ mm.

and also generate global anisotropic (orientation-dependent) mechanical behavior in the scale assembly.

The fish engages in both convex and concave bending during its normal undulatory motion[27]. We choose to look at concave bending, since scale-to-scale contacts generate greater resistance to bending. The two lowest stiffness orientations, $\varphi = 90°$ and $\varphi = 60°$, correspond to the two commonly observed bending modes in the fish: axial bending and torsion, respectively[27,28]. In these orientations, the interserial sliding mechanism allows the assembly to bend under a small applied load without generating interscale contacts or introducing stress concentrations within the scales in the initial phase of deformation. In the 90° orientation, all strains are sustained in the substrate up to 36% deformation (40 vertical mm / 112 mm total sample height), and sample stiffness matches that of the control sample without any scales. Since the rigid scales are "mechanically invisible" and do not

contribute any resistance to bending, we show that it is possible to use shape as a materials design parameter to create composite materials that provide added protection from the stiffer material (e.g., scales) while maintaining the low bending stiffness of the compliant material (e.g., substrate). In the 60° orientation, all strains are sustained in the substrate up to 4.5% deformation, after which the orientation of scales relative to the loading direction allows the interscale contacts to utilize low stiffness interscale mobility mechanisms (i.e., coupled paraserial and interserial rotation), to continue to enable interserial sliding of scales.

The high stiffness orientations correspond to bending modes in which the fish does not engage; for instance, 150° represents dorso-ventral bending about a horizontal plane through the middle of the fish. Thus, the complex geometry and orientation of scales enables flexibility of the integument in directions that it

uses for axial bending and torsion, and restricts flexibility in the directions it does not need. Features such as the oblong anterior process and concave anterior margin that make contact with the substrate and interlock with neighboring scales to provide full-body coverage of scales over the dermis as the scales move apart from each other, e.g., in ventral scales that splay apart from each other since they are oriented away from the plane of axial bending or torsion[29], and in scales that slide apart during convex bending.

Understanding complex materials-morphometric design rules in natural exoskeletons and translating them to synthetic designs holds tremendous application for bio-inspired flexible armor[16,36]. By creating flexible composite prototypes inspired by the scale armor of *P. senegalus*, we have generated one design scheme that exhibits a wide array of mechanical behavior with bending stiffness ranging over several orders of magnitude ($K = 1$–450), thus showing how morphometry can tune the flexibility of protective, composite architectures without varying the constituent materials or their volume fraction. Our concurrent and future work seeks to integrate morphometric heterogeneity[29,33], ability to conform to arbitrary curved surfaces[33], and intrascale material heterogeneity[37] into the prototype design for a truly hierarchical design that replicates all aspects of the biological armor. Biomimetic armors utilizing a segmented design hold enormous potential for a wide variety of applications by allowing damage localization, flexibility, reduced cost of fabrication, and selective replacement of damaged units.

Methods

Fish scale extraction and 3D reconstruction. Scales were surgically excised from a live *P. senegalus* specimen (219 mm body length). The specimen was anesthetized with 0.03 wt.% solution of tricaine methanesulfonate (MS-222, Sigma Aldrich) in water neutralized with potassium hydroxide. Four scales were removed from the 49th column on the left flank of the specimen with sterile, surgical-grade scalpels. The fish was transferred to anesthetic-free water to recover, and then returned to a quarantine aquarium and treated with tetracycline antibiotics (250 mg per 10 gallons of water per day) for two weeks until the scales began to regenerate. All work with the live specimen was performed in accordance with MIT's Committee on Animal Care and IACUC regulations. The excised scales were scanned using x-ray microtomography (μCT) and reconstructed as tessellated surface files (STL) following our previously published procedure[29]. Two neighboring scales were segmented into halves and reassembled into one "unitized" scale geometry (Fig. 1a) that can be assembled in tiled arrangements. The unitized scale geometry is tiled over the surface to study the geometrical principles of scale articulation (Fig. 1b). We then chose the main geometrical features to mimic in the 3D modeling of the biomimetic scale design: peg (P), socket (S), anterior process (AP), anterior shelf (AS), concave anterior margin (AM), and a thickened axial ridge (AR).

Computational 3D modeling of prototypes. Geometric morphometric analysis was used to define the geometry of the scale and its features from the 3D scale object following our previously published procedure[29]. Parametric CAD software (SOLIDWORKS®, Dassault Systèmes SolidWorks Corp., France) was used to design an abstracted 3D model of the scale geometry of 20 mm length with an overall rhomboid shape allowing for a tapered overlap area between scales, a tetrahedral peg, and a corresponding inverted concave socket. Associative modeling was used to replicate the individual scale geometry into square arrays with 1 mm spacing in the paraserial and interserial directions. The soft tissue substrate was modeled as a separate layer. Connective elements were modeled between the peg and socket of adjacent scales and between the scales and the substrate as additional layers. The prototypes used for measuring radius of curvature were designed as square arrays of 72 scales of 20 mm atop the substrate. The prototypes for the bending experiment were designed as 112×124 mm arrays of 20 mm scales with rigid rods of 10 mm diameter at the top and bottom of the sample. The prototype designs were exported as separate STL files for the rigid components (scale, rods) and soft components (substrate, connective elements).

Multi-material 3D printing. The prototypes were fabricated as a flexible array of scales via multi-material 3D printing (OBJET Connex500™, Stratasys, USA). The STL files for the prototype were imported into OBJET Studio software and assigned to commercially available UV-cured photopolymer materials: the rigid components were printed with VeroWhite (hard plastic with elastic modulus (E) = 2.0 GPa[34,35]), and the soft components were printed with TangoPlus (rubber-like elastomer with E = 0.63 MPa[34,35]). The print jobs were submitted using the digital printing mode at 30 μm resolution. Print support material was removed with a water jet and manual brushing.

Curvature experiment. The radius of curvature of the prototype under self-weight was examined by draping the prototype over a curved, half-cylinder mold (radius $R_m = 120$ mm) without the application of an external load, with a camera situated along the mold's axis of zero curvature. The prototype was rotated over the mold by an angle $\alpha = 0$–180°, where $\alpha = 0$° corresponds to the paraserial peg-and-socket axis in line with the mold's axis of zero curvature, and $\alpha = 90$° corresponds to the paraserial axis in line with the mold's axis of curvature. In each orientation, normal projection rods were inserted into three scales on a single line parallel to the mold's axis of curvature, and the radius of curvature of the prototype (R_p) was measured by drawing a circle amongst points of connection between the normal rod and the scales. The experiment was repeated with three samples ($N = 3$).

Bending experiment. Prototypes were designed for mechanical testing in bending with rigid rods at the top and bottom of the assembly and with scales aligned in orientation angles (φ) of 0°, 30°, 60°, 90°, 120°, and 150°, where φ is defined as the angle between the peg-and-socket axis and the loading direction. A control sample consisting of a solid TangoPlus sheet with no scales was printed as a control sample. The prototypes were experimentally tested in bending induced by axial compression on a mechanical tester (Zwick Z010, Zwick Roell, Germany) using load cells ranging from 20 to 2500 N. Sample holders were designed, 3D-printed, and affixed to the load cell with Permacel (Nitto) tape for pin–pin boundary conditions that allow rod rotation about the x-axis and constrain rotation about the y- and z-axes to prevent global twisting of the sample. The samples were induced to deform concavely (scales facing in) by setting an initial lateral deflection of 1 mm and zeroing the force before displacement-controlled compressive loading at a strain rate of 1 mm/s. The reaction force (F) vs. vertical displacement (d) for the prototypes was measured, and the experiment performed with three samples ($N = 3$) per orientation. Sample stiffness (K) was calculated as the slope of the loading curve and normalized by the stiffness of the control sample consisting of a 4.4 mm sheet of TangoPlus without scales ($K = 7.22$ N/m).

Finite element modeling. Three parts were designed for the model using FE software (ABAQUS, Dassault Systemes, France) and meshed with C3D4 (standard, linear stress) elements: a simplified scale geometry, a substrate material, and rigid rods. VeroWhite was modeled as an isotropic linear elastic material ($E = 2.0$ GPa, $v = 0.43$, and $\rho = 1.175$ g/cm³) and assigned to the scales and rigid rods. TangoPlus was modeled as a Neo-Hookean hyperelastic material (C11 = 0.63 MPa and D1 = 10^{-6}) and assigned to the substrate. The TangoPlus interconnections between the peg and socket of adjacent scales were modeled as springs with a stiffness of 0.63 MPa. Pin–pin boundary conditions were applied to the model to match the experimental conditions, and concave bending was simulated as a displacement-controlled compressive loading to induce lateral bending of the sample. Force–displacement (F–d) curves were generated as a measure of the reaction force vs. vertical displacement of the top rod at every increment. Values for stiffness (K) were calculated as the slope of the F–d data and normalized by the stiffness of a control model consisting of a 4.4 mm sheet of TangoPlus without scales ($K = 10.7$ N/m). Stresses (Mises, linear elastic, averaged) were captured through the whole model at every 10 increments.

Data availability statement

The data that support the findings of this study will be provided by the corresponding author upon reasonable request.

Code availability statement

The code that support the findings of this study will be provided by the corresponding author upon reasonable request.

References

1. Raabe, D., Sachs, C. & Romano, P. The crustacean exoskeleton as an example of a structurally and mechanically graded biological nanocomposite material. *Acta Mater.* **53**, 4281–4292 (2005).
2. Barbakadze, N., Enders, S., Gorb, S. & Arzt, E. Local mechanical properties of the head articulation cuticle in the beetle *Pachnoda marginata* (Coleoptera, Scarabaeidae). *J. Exp. Biol.* **209**, 722–730 (2006).
3. Yourdkhani, M., Pasini, D. & Barthelat, F. Multiscale mechanics and optimization of gastropod shells. *J. Bionic Eng.* **8**, 357–368 (2011).
4. Wyneken, J., Godfrey, M. H. & Bels, V. *Biology of Turtles: From Structures to Strategies of Life*. (CRC Press, 2007).

5. Krauss, S., Monsonego-Ornan, E., Zelzer, E., Fratzl, P. & Shahar, R. Mechanical function of a complex three-dimensional suture joining the bony elements in the shell of the red-eared slider turtle. *Adv. Mater.* **21**, 407–412 (2009).

6. Porter, M. M., Novitskaya, E., Castro-Ceseña, A. B., Meyers, M. A. & McKittrick, J. Highly deformable bones: unusual deformation mechanisms of seahorse armor. *Acta Biomater.* **9**, 6763–6770 (2013).

7. Porter, M. M., Adriaens, D., Hatton, R. L., Meyers, M. A. & McKittrick, J. Why the seahorse tail is square. *Science* **349**, aaa6683 (2015).

8. Bruet, B. J. F., Song, J., Boyce, M. C. & Ortiz, C. Materials design principles of ancient fish armour. *Nat. Mater.* **7**, 748–756 (2008).

9. Song, J. et al. Quantitative microstructural studies of the armor of the marine threespine stickleback (*Gasterosteus aculeatus*). *J. Struct. Biol.* **171**, 318–331 (2010).

10. Song, J., Ortiz, C. & Boyce, M. C. Threat-protection mechanics of an armored fish. *J. Mech. Behav. Biomed. Mater.* **4**, 699–712 (2011).

11. Ortiz, C. & Boyce, M. C. Bioinspired structural materials. *Science* **319**, 1053–1054 (2008).

12. Dunlop, J. W. C., Weinkamer, R. & Fratzl, P. Artful interfaces within biological materials. *Mater. Today* **14**, 70–78 (2011).

13. Wainwright, S. A. *Mechanical Design in Organisms*. (Princeton Univ. Press, 1982).

14. Weiner, S. & Addadi, L. Design strategies in mineralized biological materials. *J. Mater. Chem.* **7**, 689–702 (1997).

15. Meyers, M. A., Chen, P.-Y., Lin, A. Y.-M. & Seki, Y. Biological materials: structure and mechanical properties. *Prog. Mater. Sci.* **53**, 1–206 (2008).

16. Yang, W. et al. Natural flexible dermal armor. *Adv. Mater.* **25**, 31–48 (2013).

17. Li, Y., Ortiz, C. & Boyce, M. C. Stiffness and strength of suture joints in nature. *Phys. Rev. E* **84**, 062904 (2011).

18. Li, Y., Ortiz, C. & Boyce, M. C. Bioinspired, mechanical, deterministic fractal model for hierarchical suture joints. *Phys. Rev. E* **85**, 031901 (2012).

19. Li, L. & Ortiz, C. Biological design for simultaneous optical transparency and mechanical robustness in the shell of *Placuna placenta*. *Adv. Mater.* **25**, 2344–2350 (2013).

20. Sherman et al. Microstructural and geometric influences in the protective scales of *Atractosteus spatula*. *J. R. Soc. Interface* **13**, 20160595 (2016).

21. Martini, R. & Barthelat, F. Stretch-and-release fabrication, testing and optimization of a flexible ceramic armor inspired from fish scales. *Bioinspir. Biomim.* **11**, 066001 (2016).

22. Martini et al. A comparative study of bio-inspired protective scales using 3D printing and mechanical testing. *Acta Biomater.* **55**, 360–372 (2017).

23. Browning, A., Ortiz, C. & Boyce, M. C. Mechanics of composite elasmoid fish scale assemblies and their bioinspired analogues. *J. Mech. Behav. Biomed. Mater.* **19**, 75–86 (2013).

24. Connors, M. J. et al. Three-dimensional structure of the shell plate assembly of the chiton *Tonicella marmorea* and its biomechanical consequences. *J. Struct. Biol.* **177**, 314–328 (2012).

25. Sire, J.-Y. From ganoid to elasmoid scales in the actinopterygian fishes*. *Neth. J. Zool.* **40**, 75–92 (1989).

26. Daget, J., Gayet, M., Meunier, F. J. & Sire, J.-Y. Major discoveries on the dermal skeleton of fossil and recent polypteriforms: a review. *Fish Fish* **2**, 113–124 (2001).

27. Gemballa, S. & Bartsch, P. Architecture of the integument in lower teleostomes: functional morphology and evolutionary implications. *J. Morphol.* **253**, 290–309 (2002).

28. Tytell, E. D. & Lauder, G. V. The C-start escape response of *Polypterus senegalus*: bilateral muscle activity and variation during stage 1 and 2. *J. Exp. Biol.* **205**, 2591–2603 (2002).

29. Varshney, S., Song, J., Li, Y., Boyce, M. C. & Ortiz, C. Morphometric structural diversity of a natural armor assembly investigated by 2D continuum strain analysis. *J. Struct. Biol.* **192**, 487–499 (2015).

30. Pearson, D. M. Functional aspects of the integument in polypterid fishes. *Zool. J. Linn. Soc.* **72**, 93–106 (1981).

31. Rudykh, S. & Boyce, M. C. Analysis of elasmoid fish imbricated layered scale-tissue systems and their bio-inspired analogues at finite strains and bending. *IMA J. Appl. Math.* **79**, 830–847 (2014).

32. Rudykh, S., Ortiz, C. & Boyce, C. M. Flexibility and protection by design: imbricated hybrid microstructures of bio-inspired armor. *Soft Matter* **11**, 2547–2554 (2015).

33. Duro-Royo, J. et al. MetaMesh: a hierarchical computational model for design and fabrication of biomimetic armored surfaces. *Comput.-Aided Des.* **60**, 14–27 (2015).

34. Lin, E., Li, Y., Ortiz, C. & Boyce, M. C. 3D printed, bio-inspired prototypes and analytical models for structured suture interfaces with geometrically-tuned deformation and failure behavior. *J. Mech. Phys. Solids* **73**, 166–182 (2014).

35. Lin, E., Li, Y., Weaver, J. C., Ortiz, C. & Boyce, M. C. Tunability and enhancement of mechanical behavior with additively manufactured bio-inspired hierarchical suture interfaces. *J. Mater. Res.* **29**, 1867–1875 (2014).

36. David, N. V., Gao, X.-L. & Zheng, J. Q. Ballistic resistant body armor: Contemporary and prospective materials and related protection mechanisms. *Appl. Mech. Rev.* **62**, 050802–050802 (2009).

37. Araya, S. et al. Bioinformed performative composite structures: from biological micro-structures to material composites and articulated assemblies, *ECAADe* **31**, 575–584 (2013).

Author contributions

K.Z. and S.R. modeled and 3D-printed the prototypes; K.Z. and S.V. designed the experimental tests on the prototypes, analyzed data, and wrote the manuscript; S.V. performed the finite element modeling; E.M.A. assisted with data interpretation and manuscript preparation; M.D., M.C.B., and C.O. advised on all aspects of the research and manuscript. S.V. and K.Z. contributed equally to the study. All authors discussed the results and commented on the manuscript.

Competing interests

C.O., M.C.B., and S.H.R. are coinventors on patent US8978535 "Articulating protective system for resisting mechanical loads" (Date of Patent March 17, 2015) which relates to the current work. The authors have no other competing interests as defined by Springer Nature, or other interests that might be perceived to influence the results and/or discussion reported in this article.

Additional information

Supplementary information The online version contains supplementary material available at https://doi.org/10.1038/s43246-021-00140-3.

Correspondence and requests for materials should be addressed to C.O.

Peer review information Primary handling editor: John Plummer.

Reprints and permission information is available at http://www.nature.com/reprints

Publisher's note Springer Nature remains neutral with regard to jurisdictional claims in published maps and institutional affiliations.